2020-4

Effect of Ho^{3+} Ion Doping on Thermal, Structural, and Morphological Properties of Co–Ni Ferrite Synthesized by Sol-Gel Method

D. V. Phugate, Rameshwar B. Borade, S. B. Kadam, L. A. Dhale, R. H. Kadam, Sagar E. Shirsath & A. B. Kadam

Journal of Superconductivity and Novel Magnetism

ISSN 1557-1939

J Supercond Nov Magn
DOI 10.1007/s10948-020-05616-w

Springer

Journal of Superconductivity and Novel Magnetism
https://doi.org/10.1007/s10948-020-05616-w

ORIGINAL PAPER

Effect of Ho^{3+} Ion Doping on Thermal, Structural, and Morphological Properties of Co–Ni Ferrite Synthesized by Sol-Gel Method

D. V. Phugate[1] · Rameshwar B. Borade[2] · S. B. Kadam[3] · L. A. Dhale[4] · R. H. Kadam[5] · Sagar E. Shirsath[6,7] · A. B. Kadam[8]

Received: 21 May 2020 / Accepted: 18 July 2020

Abstract
Rare earth Ho^{3+}-substituted Co–Ni ferrites having a chemical formula $Co_{0.6}Ni_{0.4}Fe_{2-x}Ho_xO_4$ (0.0, 0.025, 0.05, 0.075, and 0.1) were prepared via sol-gel route. The phase formation of these samples was confirmed by the thermogravimetric analysis with differential thermal analysis and X-ray powder diffraction techniques. Rietveld refinement confirms the cubic spinel structure of the prepared samples having space group Fd3− m with presence of secondary phase of α-Fe_2O_3. The lattice parameter is increased from 8.412 to 8.582 Å with Ho^{3+} ion concentration in cobalt–nickel ferrite from $x = 0$ to $x = 0.1$. The distribution of cations has been studied with the help of X-ray diffraction data and it is found that Ho^{3+} ions preferred to occupy the octahedral [B] site. The other structural parameters like X-ray density, bulk density, hopping length, and allied parameter are increased with the composition of Ho^{3+} ions in the Co–Ni ferrite. The morphology of the samples was observed by transmission electron microscopy and scanning electron microscopy showed the nanostructured formation.

Keywords Ho-substituted Co–Ni ferrite · Rietveld refinement · Cation distribution · Morphology · Sol-gel method

1 Introduction

Cobalt–nickel (Co–Ni) ferrite is a ferrimagnetic material that presents the highest magnetocrystalline anisotropy and magnetostriction coefficient among ferrites. It has been regarded as one of the competitive candidates for different uses in high-density recording media, microwave devices, high sensitivity sensors, and biomedical industries [1–4]. The general formula for spinel ferrite is $(M^{2+})[Fe_2^{3+}]O_4^{2-}$, in which M^{2+} is divalent and Fe^{3+} is trivalent cations. It has face-centered cubic structure and having space group Fd-3m. The lattice has two interstitial sites; tetrahedral (A) and octahedral [B] which are formed by close-packed face-centered cubic array of anions. In this, half of Fe^{3+} ions are occupied at tetrahedral (A) site and the remaining half with M^{2+} ions are occupied at octahedral [B] site [5, 6]. The structural properties of ferrites can be modified by doping rare earth (RE) metal ions which have attracted the attention of researchers [7]. Since, the magnetic behavior of the ferromagnetic oxides is largely governed by the Fe–Fe interaction (the spin coupling of the 3d electrons) and by introducing rare earth (RE) metal ions in the ferrite lattice, the RE–Fe interactions may start to have an appreciable effect (3d–4f coupling), which can lead to altering the magnetization and Curie temperature. However, the RE–RE interactions are very weak since their results from the indirect mechanism 4f–5d–5d–4f [8]. There are a few reports available that have mentioned the synthesis of rare earth (RE^{3+}) substituted nanocrystalline spinel ferrites in single-phase form using different chemical routes despite having a big difference in ionic radius of RE^{3+} and Fe^{3+} ions [9–14].

✉ A. B. Kadam
drabkadam@gmail.com

1 Department of Physics, Shivaji College, Omerga, Osmanabad, MS, India

2 Department of Physics, MSS's Arts, Science and Commerce College, Ambad, Jalna, MS 431204, India

3 Department of Physics, Lal Bahadur Shastri College, Partur, Jalna, MS 431501, India

4 Department of Chemistry, Shrikrishna College, Gunjoti, Omerga, Osmanabad, MS, India

5 Materials Science Research Laboratory, Shrikrishna Mahavidyalaya, Gunjoti, Osmanabad, MS 413613, India

6 Department of Physics, Vivekanand College, Aurangabad, MS 431001, India

7 School of Materials Science and Engineering, University of New South Wales, Sydney, NSW 2052, Australia

8 Department of Physics, Jawahar Art Science and Commerce College, Andur, Osmanabad, MS 413601, India

Published online: 25 July 2020

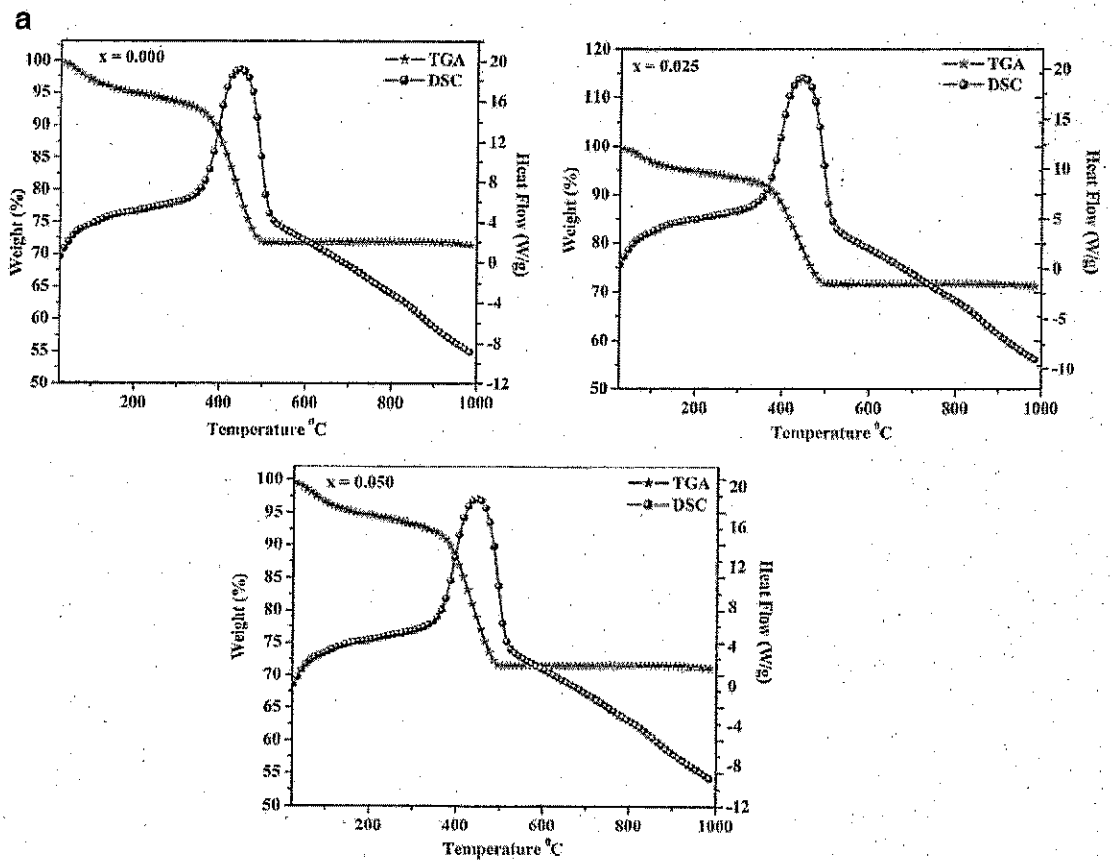

Fig. 1 a Thermo Gravimetric (TGA) and Differential Scanning Calorimetric (DSC) decomposition pattern of $Co_{0.6}Ni_{0.4}Fe_{2-x}Ho_xO_4$ ($x = 0.000$, 0.025 and 0.05), b Thermo gravimetric (TGA) and differential scanning calorimetric (DSC) decomposition pattern of $Co_{0.6}Ni_{0.4}Fe_{2-x}Ho_xO_4$ ($x = 0.075$ and 0.1)

Nanosize particles of ferrites can be prepared using various synthesis techniques, namely, citrate precursor [15], hydrothermal [16], co-precipitation [17], microemulsion [18], and sol-gel method [19]. Recently, among these methods, the sol-gel auto-combustion method has received much interest, because of its many advantages for preparing ferrite materials. It is a simple process with excellent control of the stoichiometry, and a homogeneous material with small grain size. Ferrite can be formed over a large area via the sol-gel method at a relatively low processing temperature [20, 21].

In this work, the Ho-substituted Co–Ni ferrites having chemical composition $Co_{0.6}Ni_{0.4}Fe_{2-x}Ho_xO_4$ ($x = 0.0$, 0.025, 0.05, 0.075, and 0.1) have been fabricated and investigated. The present series was synthesized via the sol-gel auto combustion technique. The prepared samples were characterized by various characterization techniques. Thermo-gravity and differential thermal analysis (TG-DTA), X-ray diffraction (XRD), X-ray electron diffraction analysis (EDAX), transmission electron microscopy (TEM), and scanning electron microscopy (SEM) were carried out to study the effect of Ho^{+3} ion substitution on the properties of Co–Ni ferrite.

2 Experimental

2.1 Synthesis

The nanocrystalline Ho^{+3}-substituted Co–Ni ferrite having chemical composition $Co_{0.6}Ni_{0.4}Fe_{2-x}Ho_xO_4$ ($x = 0.0$, 0.025, 0.05, 0.075 and 0.1) was synthesized by sol-gel route. The pure (99%) AR grade nitrates (ferric nitrate ($Fe(NO_3)_3{\cdot}9H_2O$), cobalt nitrate ($Co(NO_3)_2{\cdot}3H_2O$), nickel nitrate ($Ni(NO_3)_2{\cdot}6H_2O$), holmium nitrate ($Ho(NO_3)_3{\cdot}5H_2O$), and citric acid ($C_6H_8O_7{\cdot}H_2O$)) were used to prepare precursor solutions of the samples. The citric acid and metal nitrates were mixed and dissolved together in a required amount of distilled water to get a clear solution. Ammonia solution was added dropwise to adjust the pH ≈ 7. This precursor mixture was heated at 90 °C on a hot plate in order to transform into a gel. This gel was heated at around 250 °C to the initiation of the gel and converted into fluffy loose powder. According to TG/DTA, all the as-combusted sample powders were annealed at 600 °C for 4 h to get better crystallinity.

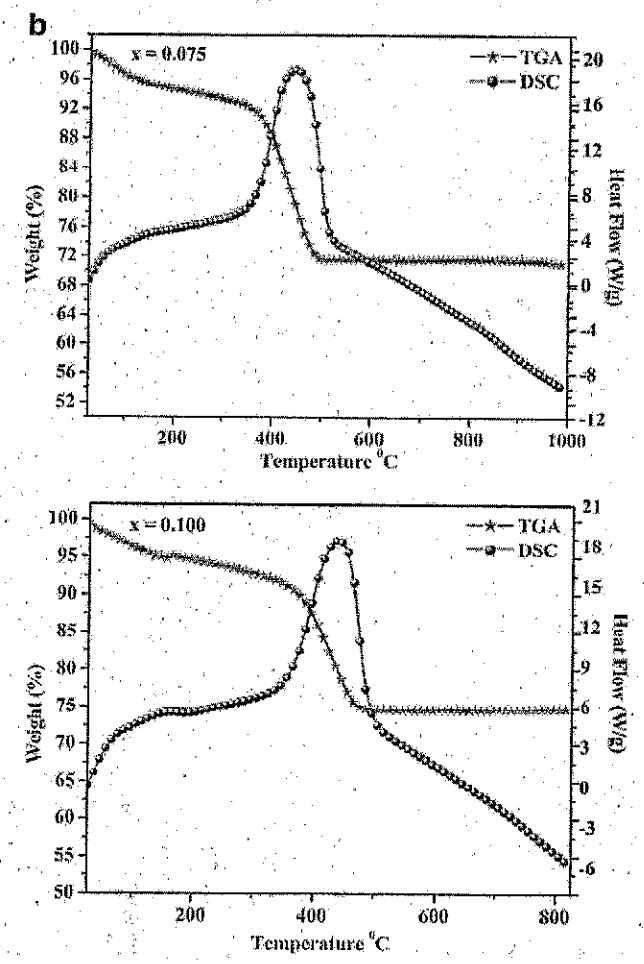

Fig. 1 (continued)

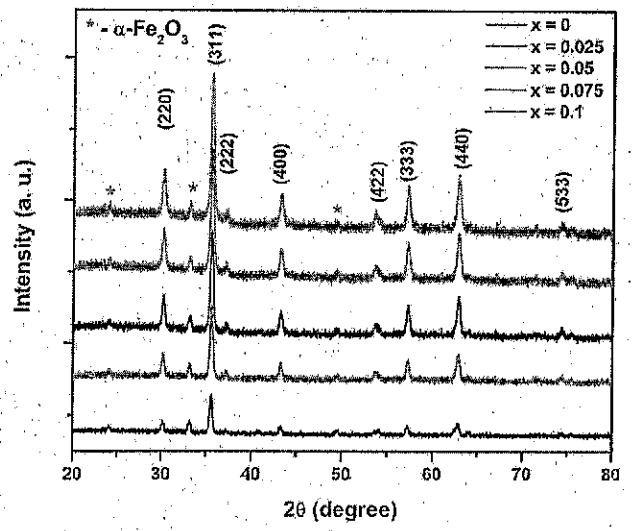

Fig. 2 XRD patterns $Co_{0.6}Ni_{0.4}Fe_{2-x}Ho_xO_4$ ($x = 0.000$, 0.025, 0.050, 0.075, and 0.100)

2.2 Characterization Techniques

The as-combusted powder was characterized via TGA/DSC at a rate of 10 °C/min in nitrogen (N_2) atmosphere to decide the crystallization temperature by using Shimadzu SDT Q600 thermal analyzer. The XRD patterns of the samples have been recorded with the help of the Rigaku MiniFlex X-ray diffractometer using Cu–K_α (λ = 1.5405 Å) radiation. The morphological study carried out by scanning electron micrograph (SEM) and was recorded using the EDAX Oxford EDAX JEOL–JSM–5600 N. Transmission electron microscope (TEM) measurements were recorded on Philips (Model CM 200).

3 Results and Discussion

3.1 Thermal Decomposition

Thermogravimetric analysis and differential scanning calorimetric studies of nanoferro spinel with chemical composition $Co_{0.6}Ni_{0.4}Fe_{2-x}Ho_xO_4$ ($x = 0.000$ to 0.100), from 10 to 1000 °C, as shown in Fig. 1(a) and (b). There are three major total mass loss observed in the graph. In the first step, a mass loss of 8.47 % is observed around 110 °C which is supported by the DSC curve. The DSC curve shows an endothermic peak indicating the loss of hydrated water molecules resent at the surface of ferrite particles.. The second step shows a mass loss of 18.74% and the corresponding endothermic peak at 227 °C indicated in the DSC curve, due to the conversion of metal hydroxides to metal oxides, i.e., removal of crystalline water molecules from the ferrite particles. Further, in the third step, mass loss of 15.21% is observed near 563 °C; this step clearly shows the formation of metal oxides to metal ferrites with loss of oxygen [22]. The decomposition of samples was completed at around 570 °C. Therefore, all the prepared samples were sintered at the temperature of 600 °C.

3.2 X-Ray Diffraction

The XRD pattern of the synthesized nanoparticles is shown in Fig. 2. The planes observed in XRD are corresponding to the standard structure of spinel ferrites [ICDD # (01-074-2403)] [23]. All the samples of Ho-substituted Co–Ni ferrite have spinel cubic structure. However, Co–Ni ferrite and Ho-substituted Co–Ni ferrite are formed with the secondary phase of α-Fe_2O_3 (JCPDS 33-0664). The secondary phase is formed during the sintering process, and this formation depends on the sintering temperature. It is observed that phase formation depends on the concentration of RE metal ions; Ho^{3+} in Co–Ni ferrites

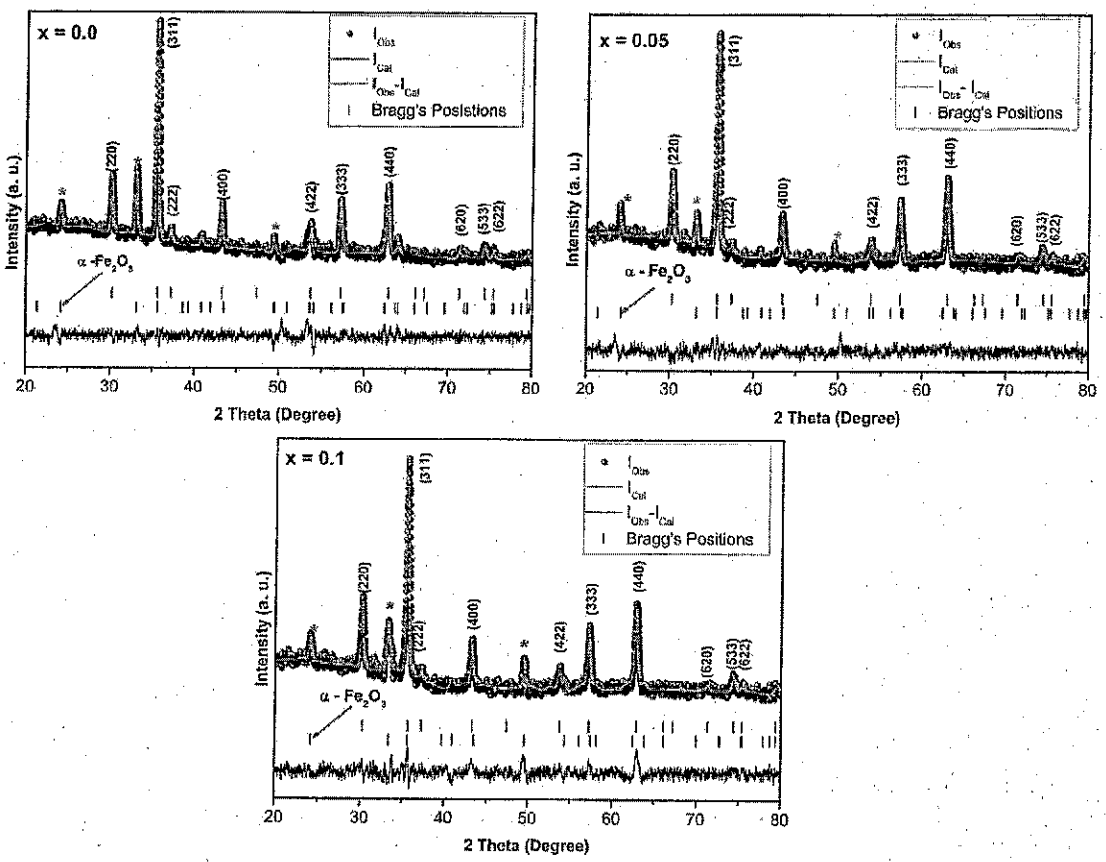

Fig. 3 Rietveld refined XRD patterns $Co_{0.6}Ni_{0.4}Fe_{2-x}Ho_xO_4$ ($x = 0$, 0.05, and 0.1)

and sintering temperature [24, 25]. The amount of Ho^{3+} composition in Co–Ni is very small; therefore, it is successfully dissolved in the spinel structure. This indicates that the secondary phase is induced due to the temperature. The most substantial reasons for the phase formation in the Ho^{3+}-substituted Co–Ni ferrite samples are electronic configuration and ionic radii of Ho^{3+} RE metal ions and host ions. The substitution of Ho^{3+} ($6s^24f^{11}$) ion in place of Fe^{3+} ($3p^63d^5$) ion will distort the lattice and influence the 3d–4f coupling. This distortion observed in the lattice is due to the increase of bond angle RE^{3+}–O^{2-}–Fe^{3+} [13]. It is known that rare earth metal ions generally prefer to occupy at octahedral B site because of their large ionic radii. The Ho^{3+} ion has a larger radius (1.04 Å) and preferred to reside at the octahedral site in place of Fe^{3+} ion whose ionic radius is 0.67 Å [26]. The Rietveld refinement of all the samples was carried out by using FullProf software to determine the distribution of cation. The Rietveld refined XRD for the sample $x = 0$, $x = 0.05$, and $x = 0.1$ are shown in Fig. 3. The samples were refined by considering an Fd−3 m space group and face-centered cubic structure. The values of goodness fit (χ^2), expected values (R_{EXP}), discrepancy factor (R_{WP}), and the distribution of cation obtained from Rietveld refinement are listed in Table 1. It is noticed that the Ho^{3+} ions strongly prefer to occupy at the octahedral [B] site. For $x \geq 0.075$, Co^{2+}

Table 1 Structural parameters obtained from Rietveld Refinement $Co_{0.6}Ni_{0.4}Fe_{2-x}Ho_xO_4$ ($x = 0.000$, 0.025, 0.050, 0.075, 0.100)

"x"	Rietveld parameters				Cation distribution by Rietveld refinement	
	χ^2	R_{EXP} (%)	R_{WP} (%)	R_P (%)	(A) site	[B] site
0.0	1.401	0.939	1.1104	0.789	$(Fe)^A$	$[Co_{0.6}Ni_{0.4}Fe]^BO_4$
0.025	1.142	1.051	1.1234	0.812	$(Fe)^A$	$[Co_{0.6}Ni_{0.4}Ho_{0.025}Fe_{0.975}]^BO_4$
0.050	1.111	1.034	1.092	0.821	$(Fe)^A$	$[Co_{0.6}Ni_{0.4}Ho_{0.050}Fe_{0.950}]^B O_4$
0.075	1.216	1.005	1.109	0.836	$(Co_{0.11}Fe_{0.89})^A$	$[Co_{0.49}Ni_{0.4}Ho_{0.075}Fe_{1.035}]^B O_4$
0.1	1.273	1.014	1.141	0.857	$(Co_{0.16}Fe_{0.84})^A$	$[Co_{0.44}Ni_{0.4}Ho_{0.1}Fe_{1.06}]^B O_4$

Table 2 Lattice constant (a), X–ray density (d_x), Bulk density (d_B), Porosity (P), crystallite size (D_{XRD}), Surface Area (S) and Hoping lengths (L_A and L_B) $Co_{0.6}Ni_{0.4}Fe_{2-x}Ho_xO_4$ ($x = 0.000$, 0.025, 0.050, 0.075, 0.100)

Comp. x	a (Å)	D_{xrd} (nm)	dx (g/cm^3)	d_B (g/cm^3)	P (%)	S (m^2/g)	Hoping lengths	
							L_A (Å)	L_B (Å)
0.000	8.412	32.212	5.315	3.026	43.07	61.56	3.578	2.921
0.025	8.421	32.268	5.372	3.178	40.84	58.51	3.600	2.940
0.050	8.428	35.601	5.423	3.233	40.38	52.13	3.649	2.980
0.075	8.486	37.522	5.457	3.257	40.32	49.10	3.674	3.000
0.100	8.582	39.712	5.497	3.303	39.91	45.75	3.716	3.034

ions migrate from the octahedral [B] site to the tetrahedral (A) site by rearranging the Fe^{3+} ions.

The lattice constant "a" was determined with the help of following relation [27]:

$$a = d\sqrt{(h^2 + k^2 + l^2)} \tag{1}$$

where h, k, and l are the Miller indices of the XRD reflection peak and d is the inter-planer spacing of Bragg's planes. Table 2 shows that the lattice constant "a" is increased from 8.412 to 8.582 Å with an increase of Ho^{3+} ion substitution in cobalt–nickel ferrite. This is due to the difference in ionic radii of host and dopant ions; the radius of Fe^{3+} (0.67 Å) is smaller than the radius of Ho^{3+} (1.04 Å) [28]. The Ho^{3+} ions are entered in the spinel ferrite crystal lattice, expanding the crystal lattice that results in the increase of lattice constant [29]. The secondary phase α-Fe_2O_3 is observed at 24.15°, 33.12°, and 49.32° diffraction angles. It is observed that the peak position of the secondary phase remains the same with the substitution of Ho3+ ions in Co–Ni ferrite. Therefore, the secondary phase will not distort the lattice corresponding to the expansion or contraction. Hence, the lattice constant is independent of the secondary phase.

The average crystallite diameter "D_{XRD}" of powder was estimated from the major peak (311) of XRD with the help of the Scherrer formula [30]:

$$D_{XRD} = \frac{0.9\lambda}{B\cos\theta} \tag{2}$$

where λ is the wavelength used in XRD, B is the full width of half maximum in (2θ), and θ is the corresponding Braggs angle. The values of crystallite size are tabulated in Table 2, and it is observed that the crystallite diameter increases from 32.1 to 39.7 nm with the Ho^{3+} substitution in cobalt–nickel ferrites.

The X-ray density (d_x) was determined by the following equation [31]:

$$dx = \frac{8M}{Na^3} \tag{3}$$

where a is lattice constant, N is the Avogadro's number, and "8" is the number of molecules per unit cell. The X-ray density is increased from 5.315 to 5.497 g/cm^3 with an increase of Ho^{3+} composition (Table 2 and Fig. 4). This behavior of X-ray density is related to the molecular weight (M) and lattice parameter (a). The increase in X-ray density may be attributed to the greater atomic mass of Ho^{3+} (164.93 amu) than that of Fe^{3+} (55.85 amu). The bulk density (d_B) is calculated from the Archimedes method, and its values with Ho^{3+} substitution are summarized in Table 2 and Fig. 4. The bulk density is increased from 4.352 ($x = 0.0$) to 4.599 ($x = 0.1$) with increase of Ho^{3+} substitution. This is attributed to the production of smaller ferrite grains, which results denser sample. The substitution of Ho^{3+} in Co–Ni ferrite changes the percentage shrinkages of the size of crystallites and increases the bulk density [29].

The percentage of porosity is determined with the help of equation [32]:

$$P = \left(\frac{d_X - d_B}{d_X}\right) \times 100 \tag{4}$$

where d_B and d_X are the bulk density and X-ray density, respectively. The values of porosities of the samples are shown in Table 2. It is observed that porosity decreases with the Ho^{3+} ion concentration in Co–Ni ferrite. This is due to the behavior of both X-ray and bulk density with the concentration of Ho^{3+} ions in ferrite samples. The specific surface area (S) was

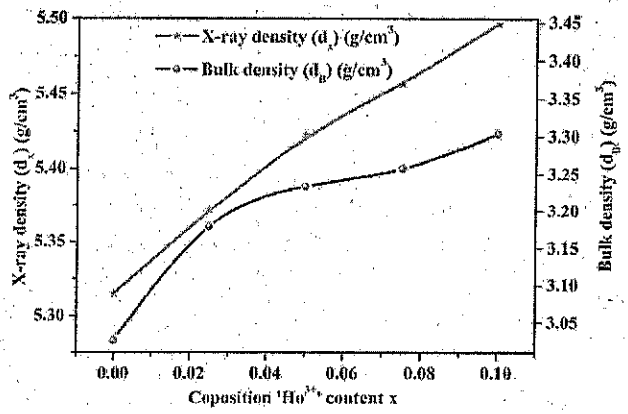

Fig. 4 Variation of X–ray density "d_x" and Bulk density "d_B" with composition "x" of Ho^{3+} ions

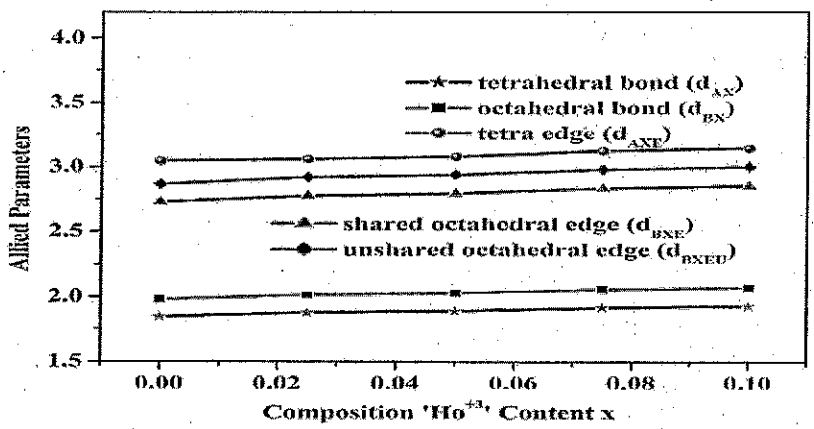

Fig. 5 Variation allied parameter with Composition "x" of Ho^{+3} ions

calculated from the crystallite size in the nanometer and the measured density in g/cm^3 using the relation [33]:

$$S = \frac{6000}{Dd_B} \tag{5}$$

where D is the crystallite size and d_B is the bulk density. The values of "S" with Ho^{3+} substitution are tabulated in Table 2. It is found that surface area decreases with Ho^{3+} ion concentration in Co–Ni ferrite. The specific surface area is inversely proportional to the bulk density and crystallite size. Since both crystallite size and bulk density are increased with Ho^{3+} substitution. Therefore, the specific surface area is decreased with Ho^{3+} composition in cobalt–nickel ferrites. Using the values of the lattice constant (a), ion jump lengths at tetrahedral (A-site) and octahedral (B-site), i.e., "L_A" and "L_B", were calculated by with the help of relations [34]:

$$L_A = a\sqrt{\frac{3}{4}} \tag{6}$$

$$L_B = a\sqrt{\frac{2}{4}} \tag{7}$$

The values of hopping lengths with Ho^{3+} ion concentration are summarized in Table 2. It is found that the hopping length of the prepared samples increases as the Ho^{3+} substitution increases. This behavior of hopping length with Ho^{3+} is analogous with the behavior of the lattice parameter with Ho^{3+} substitution. This variation could be attributed to the difference in the ionic radii of the hosts and dopant ions, which make the magnetic ions larger to each other and the hopping lengths are increased.

The allied parameters like octahedral bond and tetrahedral length, tetrahedral edge, and shared and unshared octahedral edge (d_{AXE}, d_{BXE}, and d_{BXEU}) were determined using oxygen positional parameter u (0.375 Å) and lattice parameter a,

$$d_{Ax} = a\sqrt{3}\ (u-1/4) \tag{8}$$

$$d_{Bx} = a\left[3u^2-(11/4)u+43/64)\right]^{1/2} \tag{9}$$

$$d_{AxE} = a\sqrt{2}\ (2u-1/2) \tag{10}$$

$$d_{BxE} = a\sqrt{2}(1-2u) \tag{11}$$

$$d_{BxEu} = a\left[4u^2-3u+(11/16)\right]^{1/2} \tag{12}$$

The variations of allied parameters with Ho3+ concentration in Co–Ni ferrite are shown in Fig. 5. The allied parameters are related to the radii of Ho^{3+} and Fe^{3+} ions. The allied parameters are increased with the composition of Ho^{3+} in cobalt–nickel ferrite.

3.3 Cation Distribution

Using X-ray data of the prepared samples, the cation distribution at octahedral [B] and tetrahedral (A) sites were estimated

Table 3 Composition x, cation distribution, mean ionic radii (r_A and r_B), theoretical lattice constant (a_{th}), and oxygen parameter (u) of $Co_{0.6}Ni_{0.4}Fe_{2-x}Ho_xO_4$ ($x = 0.00$, 0.025, 0.050, 0.075, and 0.10)

Comp. X	Cation distribution by Bertaut method		Mean ionic radii		a_{th} (Å)	u (Å)
	(A) site	[B] site	r_A(Å)	r_B (Å)		
0.000	$(Fe)^A$	$[Co_{0.6}Ni_{0.4}Fe]^BO_4$	0.665	0.667	8.357	0.3872
0.025	$(Fe)^A$	$[Co_{0.6}Ni_{0.4}Ho_{0.025}Fe_{0.975}]^BO_4$	0.667	0.672	8.371	0.3869
0.050	$(Fe)^A$	$[Co_{0.6}Ni_{0.4}Ho_{0.050}Fe_{0.950}]^B\ O_4$	0.668	0.678	8.385	0.3867
0.075	$(Co_{0.05}Fe_{0.95})^A$	$[Co_{0.55}Ni_{0.4}Ho_{0.075}Fe_{0.975}]^B\ O_4$	0.669	0.683	8.399	0.3865
0.100	$(Co_{0.1}Fe_{0.9})^A$	$[Co_{0.5}Ni_{0.4}Ho_{0.1}Fe]^B\ O_4$	0.699	0.688	8.412	0.3863

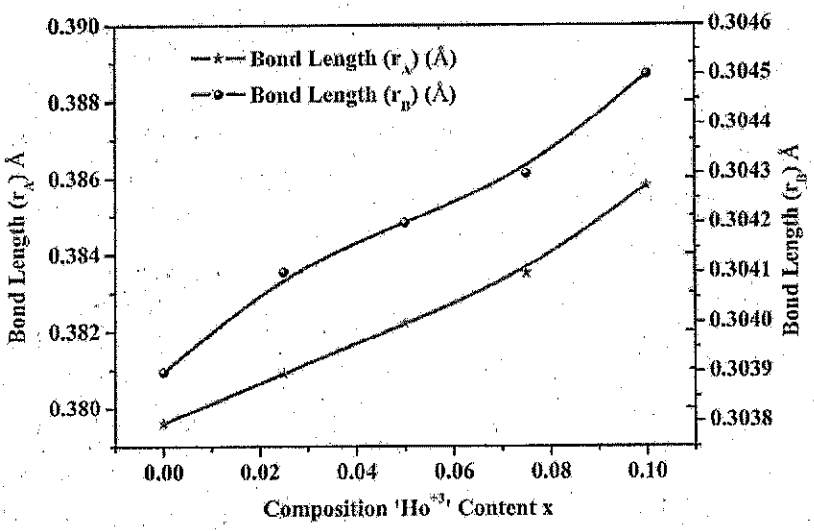

Fig. 6 Variation of Ionic Radii with Composition "x" of Ho^{+3} ions

by using Bertaut method [35]. In Bertaut method, some reflections were selected with the help of the following expression:

$$\frac{I^{Obs.}_{hkl}}{I^{Obs.}_{h'k'l'}} = \frac{I^{Cal.}_{hkl}}{I^{Cal.}_{h'k'l'}} \tag{13}$$

where $I^{Calc.}_{hkl}$ and $I^{Obs.}_{hkl}$ are the calculated and observed intensities for planes h, k, and l, respectively. By comparing observed and calculated intensity ratios of selected reflection, the distribution of cations was achieved. The oxygen parameter does not affect the intensities of the planes. In this work, the reflections of (400), (400), (420), and (422) were selected to calculate the intensity ratio. These planes are supposed sensitive to the distribution of cation. The absorption and temperature factors do not affect the calculations of intensity; therefore, these factors are not considered in the present work. The above reflections are selected by an agreement factor (R):

$$R = \left| \frac{I^{Obs.}_{hkl}}{I^{Obs.}_{h'k'l'}} - \frac{I^{Cal.}_{hkl}}{I^{Cal.}_{h'k'l'}} \right| \tag{14}$$

The intensity of a plane was calculated by the equation:

$$I_{hkl} = |F|^2_{hkl} P \cdot L_P \tag{15}$$

where P = multiplicity factor; F = structure factor; L_P = Lorentz-polarization factor and it was calculated by the formula:

$$L_P = \frac{1 + \cos^2 2\theta}{\sin^2 \cos 2\theta} \tag{16}$$

The values of the multiplicity factor, structure factor, and Lorentz-polarization factor of cations were taken from the previous literature [36]. The intensity ratio was

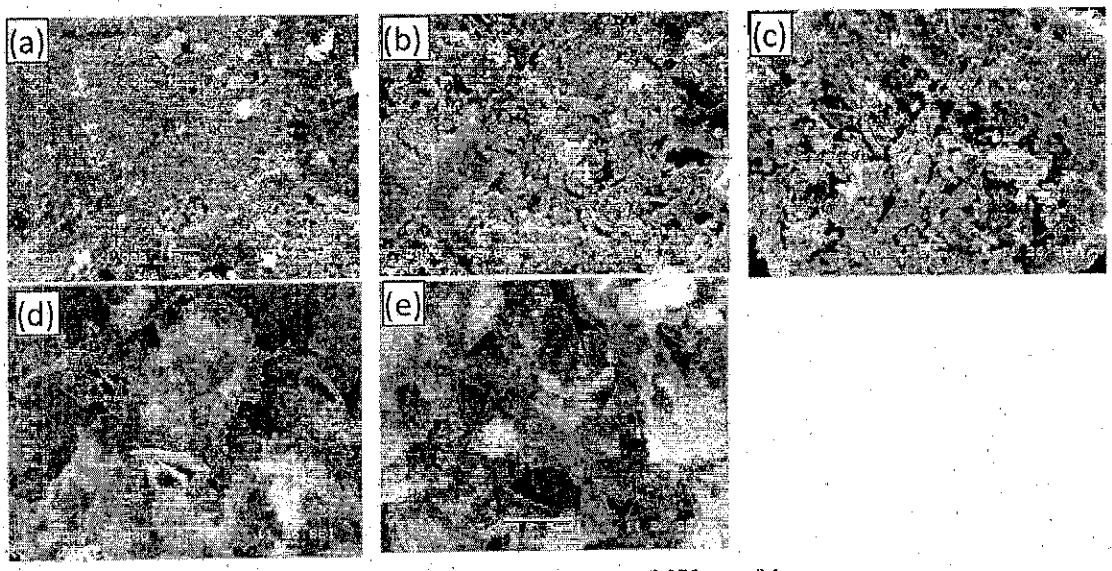

Fig. 7 SEM images of $Co_{0.6}Ni_{0.4}Fe_{2-x}Ho_xO_4$. **a** $x = 0.0$, **b** $x = 0.025$, **c** $x = 0.05$, **d** $x = 0.075$, **e** $x = 0.1$

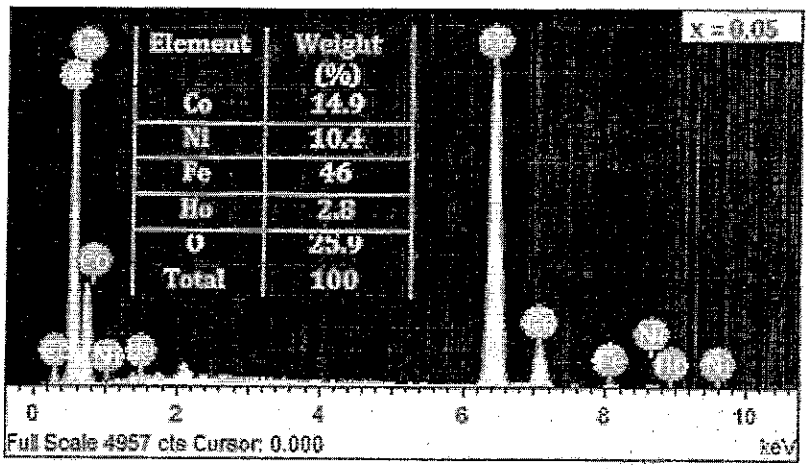

Fig. 8 EDAX spectrum of $Co_{0.6}Ni_{0.4}Fe_{2-x}Ho_xO_4$ for $x = 0.05$

calculated for the planes $I_{(440)}/I_{(422)}$, $I_{(422)}/I_{(400)}$, and $I_{(400)}/I_{(440)}$ and compared with observed relative intensity by adjusting the fraction of the cations until the agreement factor becomes minimum. The distribution of cations is listed in Table 3. It is observed that the Ho^{3+} ions prefer to reside at the octahedral site only for all the compositions of Ho^{3+}. Since the radius of the octahedral site is larger than that of a tetrahedral site in the spinel lattice. The ionic radius of the Ho^{3+} ion (1.04 Å) is larger for tetrahedral A site and therefore these larger Ho^{3+} ions occupy at the octahedral site. The substitution of Ho^{3+} cations in place of Fe3+ is preferred to occupy the octahedral sites by rearranging the cations among the octahedral and tetrahedral sites to minimize the free energy of the system. It is observed that both Co^{2+} and Ni^{2+} ions occupy in the octahedral B sites, but as the Ho^{3+} concentration increases, then Co^{2+} ions occupied in the tetrahedral A site as well. Partial migration of Co^{2+} ions (0.78 Å) from B to A sites has been observed by increasing the Ho^{3+} concentration accompanied by an opposite transfer of an equivalent number of Fe^{3+} ions (0.67 Å) from A to B sites in order to relax the strain at the octahedral sites [37]. It is noticed that the cation distribution analyzed from Rietveld refinement is the close agreement with Bertaut method. The mean ionic radii of the tetrahedral A and octahedral B sites (r_A and r_B) were determined with the help of relations discussed elsewhere [38]. The variation of ionic radii with Ho^{3+} concentration is shown in Fig. 6. It is observed that both r_A and r_B increase with an increase of Ho^{3+} substitution in Co–Ni ferrite. The increase in r_B is due to the occupancy of larger Ho^{3+} (1.04 Å) at an octahedral B site which replaced smaller Fe^{3+} (0.67 Å) ions.

The theoretical lattice parameter (a_{th}) was determined by relation [39]:

$$a_{th} = \frac{8}{3}\sqrt{3}\left[(r_A + R_0) + \sqrt{3}(r_B + R_0)\right] \tag{17}$$

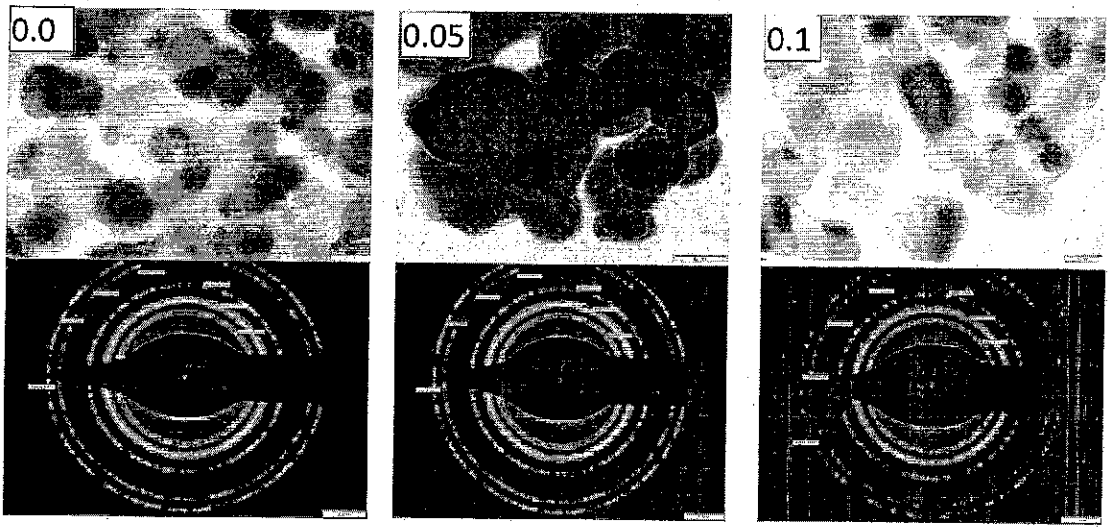

Fig. 9 TEM and their corresponding SAED image of typical sample ($x = 0.0$, 0.05 and 0.1) for $Co_{0.6}Ni_{0.4}Fe_{2-x}Ho_xO_4$

where R_O is radius of oxygen, i.e., $R_O = 1.32$ Å, and r_B and r_A are radii of octahedral [B] and tetrahedral (A) sites. The values of a_{th} are summarized in Table 3, and it is observed that theoretical lattice constant increases with an increase in Ho^{3+} substitution. This is a similar trend observed in the experimentally determined lattice parameter (a).

The oxygen positional parameter u has been determined using the radius of oxygen ion $R_O = 1.32$ Å, values of a and r_A with the help following expression [40]:

$$u = \left[(r_A + R_0)\frac{1}{\sqrt{3}a} + \frac{1}{4}\right] \quad (18)$$

The values of oxygen positional parameters are shown in Table 3, and it is found that the value of u decreases with Ho substitution in Co–Ni ferrite. In the spinel oxide, the metallic ions are smaller than the oxygen ions. The oxygen value 'u' is larger than the ideal value (0.375 Å). This value indicates that produced spinel lattice slightly deviated from the actual spinel lattice.

3.4 SEM and TEM Study

SEM micrographs were used to obtain the morphological information of the prepared Ho-substituted Co–Ni ferrite. Figure 7(a–e) shows SEM images of prepared samples. The SEM images indicate the nearly uniform distribution of grains. It is found that grains are agglomerated; therefore, it is difficult to measure the grain size of the prepared samples. Better grain boundaries were observed at the smaller substitution of Ho^{3+} ions. Compared with the XRD results mentioned above, it can be confirmed that after the addition of Ho^{3+} ions, the phase of α-Fe_2O_3 could be at grain boundaries. Further, it is observed that the grain size is decreased with Ho^{3+} substitution even though the crystallite size is increased. EDAX of typical prepared sample was carried out to study the composition of elements present in the sample. Figure 8 shows the EDAX spectra of middle composition ($x = 0.05$) of $Co_{0.6}Ni_{0.4}Fe_{2-x}Ho_xO_4$. The compositional percentage of different elements in the sample is shown in inset of Fig. 8. The presence of elements Co, Ni, Fe, Ho, and O in the spectrum is the evidence of the formation of Ho-substituted cobalt–nickel ferrite. The EDAX spectrum and inset table show that the Ho-substituted Cobalt-Nickel ferrite formed in good stoichiometric ratios.

In order to see more insight on the morphology of the prepared samples, TEM image and their corresponding SAED pattern of nano ferrite with composition $Co_{0.6}Ni_{0.4}Fe_{2-x}Ho_xO_4$ ($x = 0.0$, 0.050, and 0.1) are shown in Fig. 9. It is observed that the particles are uniformly distributed and agglomerated slightly due to magnetic interaction between the
particles. The average particle size is estimated within the range of 40–50 nm. The SAED patterns show that Ho^{3+}-doped Co–Ni ferrite nanoparticles were found in well crystalline nature. The superimposition of the bright spot with Debye ring pattern indicates the polycrystalline nature of the sample, and it is confirmed that the particles are nanometer in dimension [41, 42].

4 Conclusions

The Ho^{3+} substituted Co–Ni ferrites were synthesized by the sol-gel method. The TG-DTA graphs revealed that the decomposition prepared samples were completed around 570 °C; therefore, 600 °C may be required for the complete crystallization of samples. The structural properties like lattice constant "a" are increased from 8.412 to 8.582 Å with increasing the Ho^{3+}. The cation distribution data shows the Ho^{3+} ions is preferred to occupy the B sites and its force to Co^{2+} ions to migrate B sites to A sites, whereas Fe^{3+} ions distributed over both sites. The theoretical lattice constant is increased with an increase of Ho^{3+} ions which is in agreement with the experimental lattice constant.

References

1. Singhal, S., Singh, J., Barthwal, S.K., Chandra, K.: Preparation and characterization of nanosize nickel-substituted cobalt ferrites ($Co_{1-x}Ni_xFe_2O_4$). J. Solid State Chem. **178**(10), 3183–3189 (2005)
2. Mande, V.K., Bhoyar, D.N., Vyawhare, S.K., Jadhav, K.M.: Effect of Zn^{2+}–Cr^{3+}substitution on structural, morphological, magnetic and electrical properties of $NiFe_2O_4$ ferrite nanoparticles. J. Mater. Sci. Mater. Electron. **29**, 15259–15270 (2018)
3. Kadam, R.H., Birajdar, A.P., Gaikwad, A.S., Shirsath, S.E.: Al^{3+} ions dependent structural and magnetic properties of Co-Ni nanoalloys. J. Nanosci. Nanotechnol. **14**, 4101–4107 (2014)
4. Kadam, R.H., Birajdar, A.P., Alone, S.T., Shirsath, S.E.: Fabrication of $Co_{0.5}Ni_{0.5}Cr_xFe_{2-x}O_4$ materials via sol–gel method and their characterizations. J. Magn. Magn. Mater. **327**, 167–171 (2013)
5. Kumar, L., Kumar, P., Narayan, A., Kar, M.: Rietveld analysis of XRD patterns of different sizes of nanocrystalline cobalt ferrite. Int. Nano Lett. **3**, 8 (2013)
6. Kadam, A.B., Mande, V.K., Kadam, S.B., Kadam, R.H., Shirsath, S.E., Borade, R.B.: Influence of gadolinium (Gd^{3+}) ion substitution on structural, magnetic and electrical properties of cobalt ferrites. J. Alloys Compd. **840**, 155669 (2020)
7. Avazpour, L., Shokrollahi, H., Toroghinejad, M.R., Zandi Khajeh, M.A.: Effect of rare earth substitution on magnetic and structural properties of $Co_{1-x}RE_xFe_2O_4$ (RE: Nd, Eu) nanoparticles prepared via EDTA/EG assisted sol–gel synthesis. J. Alloys Copnd. **662**, 441–447 (2016)
8. Rezlescu, N., Rezlescu, E.: The influence of Fe substitution by R ions in a NiZn ferrite. Solid State Commun. **88**, 139–141 (1993)
9. Kahn, M.L., Zhang, Z.J.: Synthesis and magnetic properties of $CoFe_2O_4$ spinel ferrite nanoparticles doped with lanthanide ions. Appl. Phys. Lett. **78**(23), 3651–3653 (2001)

10. Shirsath, S.E., Kadam, R.H., Patange, S.M., Mane, M.L., Ghasemi, A., Morisako, A.: Enhanced magnetic properties of Dy^{3+} substituted Ni-Cu-Zn ferrite nanoparticles. Appl. Phys. Lett. **100**(4), 042407 (2012)
11. Ahmed, M.A., Ateia, E., Salah, L.M., El-Gamal, A.A.: Structural and electrical studies on La3+ substituted Ni–Zn ferrites. Mater. Chem. Phys. **92**(2–3), 310–321 (2005)
12. Ali, I., Islam, M.U., Ishaque, M., Khan, H.M., Ashiq, M.N., Rana, M.U.: Structural and magnetic properties of holmium substituted cobalt ferrites synthesized by chemical co-precipitation method. J. Magn. Magn. Mater. **324**(22), 3773–3777 (2012)
13. Bharathi, K.K., Markandeyulu, G., Ramana, C.V.: Structural, magnetic, electrical, and magnetoelectric properties of Sm-and Ho-substituted nickel ferrites. J. Phys. Chem. C. **115**(2), 554–560 (2011)
14. Manzoor, A., Khan, M.A., Shahid, M., Warsi, M.F.: Investigation of structural, dielectric and magnetic properties of Ho substituted nanostructured lithium ferrites synthesized via auto-citric combustion route. J. Alloys Compd. **710**, 547–556 (2017)
15. Verma, A., Goel, T.C., Mendiratta, R.G., Alam, M.I.: Dielectric properties of NiZn ferrites prepared by the citrate precursor method. Mater. Sci. Eng. B. **60**(2), 156–162 (1999)
16. Komarneni, S., Fregeau, E., Breval, E., Roy, R.: Hydrothermal preparation of ultrafine ferrites and their sintering. J. Am. Ceram. Soc. **71**(1), C–26 (1988)
17. Arulmurugan, R., Jeyadevan, B., Vaidyanathan, G., Sendhilnathan, S.: Effect of zinc substitution on co–Zn and Mn–Zn ferrite nanoparticles prepared by co-precipitation. J. Magn. Magn. Mater. **288**, 470–477 (2005)
18. Das, N., Majumdar, R., Sen, A., Maiti, H.S.: Nanosized bismuth ferrite powder prepared through sonochemical and microemulsion techniques. Mater. Lett. **61**(10), 2100–2104 (2007)
19. Shirsath, S.E., Wang, D., Jadhav, S.S., Mane, M.L., Li, S.: Ferrites obtained by sol-gel method. In: Klein, L., Aparicio, M., Jitianu, A. (eds.) Handbook of Sol-Gel Science and Technology, pp. 695–735. Springer, Cham (2018)
20. Mande, V.K., Kounsalye, J.S., Vyawahare, S.K., Jadhav, K.M.: Effect of γ-radiation on structural, morphological, magnetic and dielectric properties of Zn–Cr substituted nickel ferrite nanoparticles. J. Mater. Sci. Mater. Electron. **30**, 56–68 (2019)
21. Yue, Z., Zhou, J., Li, L., Zhang, H., Gui, Z.: Synthesis of nanocrystalline NiCuZn ferrite powders by sol–gel auto-combustion method. J. Magn. Magn. Mater. **208**(1–2), 55–60 (2000)
22. Toksha, B.G., Shirsath, S.E., Patange, S.M., Jadhav, K.M.: Structural investigations and magnetic properties of cobalt ferrite nanoparticles prepared by sol–gel auto combustion method. Solid State Commun. **147**(11–12), 479–483 (2008)
23. Khan, M.A., Sabir, M., Mahmood, A., Asghar, M., Mahmood, K., Khan, M.A., Ahmad, I., Sher, M., Warsi, M.F.: High frequency dielectric response and magnetic studies of $Zn_{1-x}Tb_xFe_2O_4$ nanocrystalline ferrites synthesized via micro-emulsion technique. J. Magn. Magn. Mater. **360**, 188–192 (2014)
24. Arshad, M., Asghar, M., Junaid, M., Warsi, M.F., Rasheed, M.N., Hashim, M., Khan, M.A.: Structural and magnetic properties variation of manganese ferrites via Co-Ni substitution. J. Magn. Magn. Mater. **474**, 98–103 (2019)
25. Ateia, E., Ahmed, M.A., El-Aziz, A.K.: Effect of rare earth radius and concentration on the structural and transport properties of doped Mn–Zn ferrite. J. Magn. Magn. Mater. **311**(2), 545–554 (2007)
26. Cheng, F.X., Jia, J.T., Xu, Z.G., Zhou, B., Liao, C.S., Yan, C.H., Zhao, H.B.: Microstructure, magnetic, and magneto-optical properties of chemical synthesized Co–RE (RE= Ho, Er, Tm, Yb, Lu) ferrite nanocrystalline films. J. Appl. Phys. **86**(5), 2727–2732 (1999)
27. Vinod, T., Shinde, S.S., Borade, R.B., Kadam, A.B.: Study of cation distribution, structural and electrical properties of Al–Zn substituted Ni–Co ferrite. Physica B. **577**, 411783 (2020)
28. Xi, G., Zhao, T., Wang, L., Dun, C., Zhang, Y.: Effect of doping rare earths on magnetostriction characteristics of CoFe2O4 prepared from spent Li-ion batteries. Physica B. **534**, 76–82 (2018)
29. Pachpinde, A.M., Langade, M.M., Lohar, K.S., Patange, S.M., Shirsath, S.E.: Impact of larger rare earth Pr^{3+} ions on the physical properties of chemically derived $Pr_xCoFe_{2-x}O_4$ nanoparticles. Chem. Phys. **429**, 20–26 (2014)
30. Borade, R.B., Kadam, S.B., Wagare, D.S., Kadam, R.H., Shirsath, S.E., Nimbore, S.R., Kadam, A.B.: Fabrication of Bi^{3+} substituted yttrium aluminum iron garnet (YAIG) nanoparticles and their structural, magnetic, optical and electrical investigations. J. Mater. Sci. Mater. Electron. **30**, 19782–19791 (2019)
31. Borade, R.B., Shirsath, S.E., Vats, G., Gaikwad, A.S., Patange, S.M., Kadam, S.B., Kadam, R.H., Kadam, A.B.: Polycrystalline to preferred-(100) single crystal texture phase transformation of yttrium iron garnet nanoparticles. Nanoscale Adv. **1**(1), 403–413 (2019)
32. Han, Y., Sun, A., Pan, X., Zhang, W., Zhao, X.: Effect of different sintering temperatures on Structuraland magnetic properties of Zn–Co ferrite nanoparticles. J. Supercond. Nov. Magn. **32**, 3823–3830 (2019)
33. Maksoud, M.I.A.A., El-Sayyad, G.S., Ashour, A.H., El-Batal, A.I., Elsayed, M.A., Gobara, M., El-Khawaga, A.M., Abdel-Khalek, E.K., El-Okr, M.M.: Antibacterial, antibiofilm, and photocatalytic activities of metals-substituted spinel cobalt ferrite nanoparticles. Microb. Pathog. **127**, 144–158 (2019)
34. Zhao, X., Sun, A., Zhang, W., Han, Y., Pan, X.: Effects of mg substitution on the structural and magnetic properties of $Ni_{0.2}Mg_xCo_{0.8-x}Fe_2O_4$ nanoparticle ferrites. J. Supercond. Nov. Magn. **32**, 2589–2598 (2019)
35. Shahane, G.S., Zipare, K.V., Bandgar, S.S., Mathe, V.L.: Cation distribution and magnetic properties of Zn^{2+} substituted $MnFe_2O_4$ nanoparticles. J. Mater. Sci. Mater. Electron. **28**, 4146–4153 (2017)
36. Cullity, B.D.: Elements of X-Ray Diffraction. Addison-Wesley Publishing (1956)
37. Kumar, L., Kumar, P., Kuncser, V., Greculeasa, S., Sahoo, B., Kar, M.: Strain induced magnetism and superexchange interaction in Cr substituted nanocrystalline cobalt ferrite. Mater. Chem. Phys. **211**, 54–64 (2018)
38. Routray, K.L., Saha, S., Behera, D.: Rare-earth (La^{3+}) substitution induced changes in the structural, dielectric and magnetic properties of nano-$CoFe_2O_4$ for high-frequency and magneto-recording devices. Appl. Phys. A. **125**, 328 (2019)
39. Sharma, R., Thakur, P., Sharma, P., Sharma, V.: Ferrimagnetic Ni^{2+} doped Mg-Zn spinel ferrite nanoparticles for high density information storage. J. Alloys Copnd. **704**, 7–17 (2017)
40. Al Maashani, M.S., Khalaf, K.A., Gismelseed, A.M., Al-Omari, I.A.: The structural and magnetic properties of the nano-CoFe2O4 ferrite prepared by sol-gel auto-combustion technique. J. Alloys Compd. **817**, 152786 (2020)
41. Al-Hilli, M.F., Li, S., Kassim, K.S.: Gadolinium substitution and sintering temperature dependent electronic properties of Li–Ni ferrite. Mater. Chem. Phys. **128**(1–2), 127–132 (2011)
42. Shirsath, S.E., Kadam, R.H., Mane, M.L., Ghasemi, A., Yasukawa, Y., Liu, X., Morisako, A.: Permeability and magnetic interactions in Co^{2+} substituted $Li_{0.5}Fe_{2.5}O_4$. J. Alloys Compd. **575**, 145–151 (2013)